Environment-modulated glacial seismicity near Dalk Glacier in East Antarctica revealed by deep clustering

Yanlan Hu[1], Zefeng Li*[1,2], Lei Fu*[3], Xuying Liu[4]

[1]Laboratory of Seismology and Physics of Earth's Interior, School of Earth and Space Sciences, University of Science and Technology of China, Hefei, China

[2]Mengcheng National Geophysical Observatory, University of Science and Technology of China, Mengcheng, China

[3]School of Geophysics and Geomatics, China University of Geosciences (Wuhan), Wuhan, China

[4]College of global change and earth system science, Beijing Normal University, Beijing, China

*Correspondence to: Zefeng Li (zefengli@ustc.edu.cn), Lei Fu (fulei@cug.edu.cn)

Key points:

1. We apply deep unsupervised learning to identify seismic signals near Dalk Glacier in the Larsemann Hills, East Antarctica.
2. Three types of events are associated with wind, thermal contraction/basal slip and water-filled crevassing/iceberg calving, respectively.
3. The temperature- and tide- modulated patterns of the glacial seismicity are suggestive of the susceptibility to environment conditions.

Abstract

East Antarctica constitutes two-thirds of the Antarctic continent, where glacier systems have been thought to be more stable than those in West Antarctica. However, the stability could be increasingly undermined by global warming, intensifying local and regional glacial activities. Here, using deep unsupervised learning, we analyze seismic signals recorded by a dense nodal array near Dalk glacier in the Larsemann Hills, East Antarctica, in austral summer (6 Dec 2019 – 2 Jan 2020). We apply an autoencoder to automatically extract event features and input them to a Gaussian mixture model for clustering. During the operation period, three main types of seismic signals are identified: high-frequency monochromatic events, broadband short-duration icequakes, and low-frequency long-duration events. By comparing these events to environmental observations (local wind speed, temperature, tide level, and satellite imagery), we infer that the first type was wind-induced vibration, the second type thermal contraction/basal slip, and the third type water-filled crevassing/iceberg calving. The latter two glacial activities appear to be modulated by temperature and tide, respectively, implying the susceptibility of Dalk glacier to environment conditions in East Antarctica. Our results demonstrate that deep clustering is an effective means to identify diverse glacial seismicity and contributes to the rapid growth of passive glacier seismic monitoring.

Plain Language Summary

The ice in Antarctica is accelerating to melt, fall into the sea and rise the sea level. Although East Antarctica is more stable than West Antarctica for now, the state of stability could be interrupted by global warming. Seismic monitoring is a rapidly growing means for tracking glacial activities because ice movement, fracturing and collision would all emit seismic waves. To explore glacial dynamics in East Antarctica, we investigated the seismic signals near Dalk Glacier in Larsemann Hills, East Antarctica from 6 Dec 2019 to 2 Jan 2020, using a machine learning approach. Finally, we obtain three categories and attributed them to wind-induced vibrations, thermal contraction at surface ice and/or stick-slip at ice base, and tidally modulated water-filled crevassing/iceberg calving. These results imply that the glacial activities near Dalk Glacier are susceptible to environment conditions.

1. Introduction

Global warming modifies glacial environments and leads to rising sea levels. Freshwater input to the oceans can in turn influence the global climate (Shepherd and Wingham, 2007, 2007; Rignot et al., 2008, 2019; Dutton et al., 2015; Paolo et al., 2015). Remote sensing observations reveal that the melting of global glaciers has reached a speed of 267±16 gigatons per year, contributing to 21±3% of sea-level rise in the past two decades (Hugonnet et al., 2021). Unstable glacial systems are manifested seismically as active basal motion, ice fracturing and iceberg calving, which were tracked by increasingly dense global and local seismic networks (Neave and Savage, 1970a; Qamar, 1988; Deichmann et al., 2000; Ekström et al., 2003; Podolskiy and Walter, 2016).

The involvement of multiphase media such as ice, water, snow and rock results in very diverse seismic signals, making seismic data analysis in glacial environments challenging (Neave and Savage, 1970a; Walter et al., 2008; Winberry et al., 2009; Bartholomaus et al., 2012; Röösli et al., 2014). Recent studies have shown that unsupervised learning can efficiently classify seismic data (Köhler et al., 2010; Chen, 2018; Mousavi et al., 2019; Seydoux et al., 2020; Cui et al., 2021). For example, Jenkins et al. (2021) compared two deep unsupervised frameworks, i.e., deep embedded clustering (DEC) and the Gaussian mixture model (GMM), for classifying 3-20 Hz seismic signals in the Ross Ice Shelf, West Antarctica. They observed that the highest seismicity occurred at the ice front and near grounding zones and showed seasonal and tidal patterns.

The Antarctic Ice Sheet is divided into the West Antarctic Ice Sheet, the East Antarctic Ice Sheet and the Antarctic Peninsula Ice Sheet. The East Antarctic Ice Sheet shows mass equilibrium or modest gains in recent decades, whereas the other two experience rapid mass loss (Davis et al., 2005; Zwally et al., 2005; Shepherd et al., 2018; Rignot et al., 2019). However, geological evidence and numerical modeling suggest substantial sea-level contributions from East Antarctica in past warm periods and over

the coming centuries (Cook et al., 2013; DeConto and Pollard, 2016; Wilson et al., 2018; Stokes et al., 2022). Mass loss in marine-based sectors of the East Antarctic Ice Sheet, such as Wilkes Land, have accelerated, driving deep ice destabilization and disintegration (Greenbaum et al., 2015; Mohajerani et al., 2018; Shen et al., 2018; Wang et al., 2021).

The Larsemann Hills in East Antarctica is located to the east of the Amery Ice Shelf (Figure 1a). Dalk Glacier in this region is one of the major outlets in East Antarctica and drains meltwater into the southeastern part of Prydz Bay. Dalk glacier has a mean surface velocity of approximately 170 m a^{-1} and a 3-5 year calving cycle, with the latest terminus retreat in 2016 August (Chen et al., 2020). Guo et al., (2022) found possible existence of subglacial water by ground penetrating radar, which may facilitate fluid-related activity in the area. In this study, we use deep clustering to investigate the seismic signals near Dalk Glacier. We focus on a 100-station dense seismic array in the austral summer of 2019 and identify three main categories of seismic events during the one-month operation period. The mechanisms of the seismic events are inferred from their frequency contents, temporal and spatial patterns. These results contribute to the understanding of glacial dynamics in relatively stable East Antarctica.

2. Data and Methods

During the 36th Chinese National Antarctic Research Expedition, 100 three-component short-period seismometers were deployed in the Larsemann Hills from 6 Dec 2019 to 2 Jan 2020. The seismometers have a sampling rate of 500 Hz and a corner frequency of 5 Hz. They were buried approximately 0.5 m beneath the snowy surface. Sticks with streamers were planted for the identification purpose. The array has an “L” shape with a total length of 20 km and an average spacing of 200 m (Figure 1b).

The waveforms are detrended and 1-Hz high-pass filtered. A short-term average/long-

term average (STA/LTA) algorithm is applied to each station to detect impulsive signals. We set the STA window as 0.5 s and the LTA window as 30 s. A trigger threshold of 10 and a detrigger threshold of 3 are taken. The waveforms are transformed to time-frequency spectrograms using a 1 s Hanning window (512 samples), NFFT = 512 and 90% overlapping. The resulting dimension of the spectrograms is 10,240, i.e., 256 frequencies (up to 250 Hz) and 40 time steps (4 s). Following Jenkins et al. (2021), we center the spectral peak in each spectrogram to alleviate the impact of the arrival time of the maximal amplitude. The spectrograms are normalized by energy maxima before being input into the autoencoder.

The deep clustering consists of feature extraction with an autoencoder and clustering with Gaussian mixture modeling (Figure 2). Note that in this approach, the feature extraction and the clustering are independent. Another popular approach called DEC (Deep Embedded Clustering), which is also tested by Jenkins et al. (2021), allows adjustment of the latent feature space according to clustering performance. However, in this study, we do not use DEC because the latent space might be distorted due to the feedback mechanism and the representability of the latent features could be undermined (Guo et al., 2017; Jenkins et al., 2021).

An autoencoder is one type of deep neural networks (Kramer, 1991). It encodes a spectrogram into a compact representation (or latent features) and then reconstructs the spectrogram as close as possible from the latent features by a decoder. The encoding representation has a low dimension, and therefore, the network is forced to capture the main data features. We construct the encoder as two convolutional and two fully connected layers and the decoder in reverse (Figure 2). For each convolutional layer, we set the kernel size as 5 and the stride as 3. The bottleneck dimension is a key parameter of the network. We test the choices of 8, 16, 32 and decide to use 16, as the reconstruction loss at 16 remains similar for higher dimensions. The training uses 70% of the data, and the remaining data are used for validation. Batch normalization and a dropout rate of 0.1 are applied.

After the autoencoder is trained, the latent features from the encoder are input into Gaussian mixture modeling (GMM) for clustering. GMM assumes that different clusters are drawn from different Gaussian distributions (Reynolds, 2009). It models the dataset by minimizing the loss between the data distribution and a mixture of k Gaussian distribution functions, where k is a user-defined number of clusters. We set k as 50 for overly division and then merge similar clusters manually for simplicity of interpretation.

4. Results

The STA/LTA algorithm produced 909,720 seismic detections. With 50 detailed groups by deep clustering, we manually grouped them into three large classes (Clusters A, B, and C) according to their spectral similarity (readers are referred to the supplementary materials for details; Figures S1-S3). This section describes the primary characteristics of each cluster and compares their temporal distributions with various environmental factors. The wind speed and temperature were recorded at Chinese Zhongshan station. The tide heights around Dalk Glacier front are derived from SPOTL using the CATS2008a model (Padman et al., 2002; Agnew, 2012).

4.1. Cluster A: wind-induced vibration

The 249,687 events in Cluster A have narrow frequency bands, typically at 10-20, 60-80, 90-100, or 180-200 Hz. They strongly correlate with wind speed, present when wind speed exceeds approximately 3 m/s, and thus are inferred to be wind-induced vibrations of sticks, streamers, and ground surface (Figure 3). The Spearman correlation coefficient between the occurrence counts and wind speed is 0.469. The p value is 5.6e-38, rejecting the null hypothesis that they occurred randomly.

Previous studies have shown that seismic wind noise ranges widely in frequency and amplitude, depending on deployment depth, interaction medium, topography and wind velocity (Withers et al., 1996; Mucciarelli et al., 2005; Johnson et al., 2019;

Frankinet et al., 2021). We suppose that the highest frequencies (180-200 Hz) are generated by the sticks with streamers planted near the stations and that the lower frequencies (10-20 Hz, 60-80 Hz and 90-100 Hz) are probably from wind blowing across the surface snow layer or ice. In part of the SE–NW section of the array, Cluster A events were absent (Figure 3). This was likely because this area was covered by the loose new wet snow during the deployment period, and the vibration was absorbed.

4.2. Cluster B: short-duration and broadband events

The Cluster B events are characterized by short duration (~0.5 s), impulsive and broadband energy (20-200 Hz), consistent with icequakes observed elsewhere (Neave and Savage, 1970b; Osten-Woldenburg, 1990; Podolskiy and Walter, 2016). Spatially, most of them came from very local sources near the northern array terminus and were recorded only by the northernmost station 185 (Figure S4). Temporally, the icequakes near Dalk Glacier mostly occurred in local early mornings, particularly when the temperature fell below 0 ℃.

We calculate Spearman coefficients and *p* values between the hourly event counts and local wind speed, temperature recorded at the Zhongshan station, and theoretical tide level (Figure 4). The statistical distributions of Spearman coefficients and *p* values are obtained with 1,000 random selections of 20% of data points. The bootstrapping test shows that temperature is the most relevant environmental factor compared to tide and wind (Figure 5). The mean absolute spearman coefficient is -0.33, and the mean *p* value is 5.19e-5. The tide height also has a relatively high correlation coefficient of 0.25, but the phase seems not synchronized. These observations suggest that low temperature is the probable main driving force behind the high-frequency icequakes.

4.3. Cluster C: low-frequency and hybrid events

In contrast to the local, short-duration and broadband events in Cluster B, the Cluster C events are observed across the array and dominated by low-frequency energy at 1-

10 Hz with duration >5 s. Temporally, these events are anticorrelated with wind speed (-0.28), likely because some smaller events are masked by strong wind noise. Interestingly, they appear to be correlated well with fortnight tides. Spatially, the detected events along the array exhibit a bimodal distribution: one peak at the northernmost stations and the other peak around Station 236, which is 3.8 km from the array's northern terminus (Figure 6). Accordingly, we speculate that there are two subgroups of predominant persistent sources. The events from the mid-array source exhibit preceding weak energy above 50-100 Hz before the 1-10 Hz wavetrain (Figures 7a-c). Comparatively, those from the northernmost region only show 1-10 Hz contents (Figures 7d-f). Whether this difference is a source or path effect will be discussed later.

5. Discussions and Conclusions

We have used deep clustering to group nearly a million seismic signals near Dalk glacier in East Antarctica. Three major categories of seismic signals are obtained in the region: wind-induced narrow-frequency-band episodes, local short-duration broadband events, and regional long-duration low-frequency events. The differences in their temporal and spatial distributions, as well as correlations with environmental forces, suggest different underlying dynamic processes behind them. In this section, we further discuss the possible mechanisms of latter two glacier-related seismicity, as well as the potential and limitations of the unsupervised learning method.

5.1. Mechanisms of short-duration broadband events: surface thermal contraction and basal stick-slip

The broadband nature of the Cluster B events indicates that they are likely brittle failures of solid materials. The correlation with subfreezing temperature suggests plausible association with the phase transition between ice and waterflow. Previous studies have shown that many glacial activities are more frequent during daily cold periods (Walter et al., 2008; Roeoesli et al., 2016; Lombardi et al., 2019; MacAyeal et al., 2019; Winter et al., 2021). Based on these two constraints, there could be two

candidate mechanisms.

The first is thermal contraction of the surface ice. Satellite imagery on 19 Dec 2019 (Figure 1b) shows blocks of low-reflectance exposed ice surfaces near Station 185, whereas the rest of the array was covered by high-reflectance snow. The low-reflectance surfaces are called “blue ice areas” where the surface temperature is higher in daytime (Bintanja, 1999). The larger diurnal temperature changes lead to greater local strain rates. On cold nights when the ice viscosity is high, the blue ice areas may undergo brittle failure and produce cracking signals (Butkovich, 1959; Bažant, 1992; Bøggild et al., 1995; Lombardi et al., 2019; Winter et al., 2021).

The second mechanism is stick-slip at the basal interface between ice and ice, ice and till, or ice and rock. Low temperature can inhibit sliding by decreasing the inflow of meltwater, making subglacial till rougher and refreezing the interfaces (Anandakrishnan and Bentley, 1993; Zoet et al., 2013; Roeoesli et al., 2016). Stick-slip events may then occur when the accumulated shear stress exceeds the locking friction. Speculatively, there could be asperities or “sticky spots” under Station 185 experiencing stress accumulation due to diurnal temperature variations. In particular, we observe swarms of highly repetitive icequakes within a short period of time (Figure S5). These similar icequakes implies recurrent ruptures of the same basal asperities during glacial movement (Danesi et al., 2007; Allstadt and Malone, 2014; Lipovsky and Dunham, 2016).

As these icequakes are only recorded by one or two stations, it is difficult to determine whether the sources are shallow or deep and to rule out either of the two mechanisms. Besides, an intense swarm of high-frequency events near the end of December are anomalous (Figure 4). This swarm coincided with the drainage of the lake near the Russian Progress-3 Station beginning on 8 Jan 2020 and the following overflow of neighboring lakes (Boronina et al., 2021). This seems to imply that the

high-frequency events can also be caused by instability changes in the nearby glacial systems.

5.2. Mechanisms of low-frequency and hybrid events: water-filled crevassing and iceberg calving

The cluster C events consist of two major types: one with precursory weak high frequencies (up to 150 Hz) and sequent low frequencies (1-10 Hz) with a duration of 5-10 s (Figure 7a-7c), while the other with only low frequencies (1-10 Hz) (Figure 7d-7f). The former hybrid icequakes resemble hybrid events in volcano systems, which are considered as brittle failure of rocks and subsequent fluid-filling resonance in the fractured space(Chouet, 1996). Analogously, the hybrid icequakes observed near Dalk glacier could be interpreted as brittle fracturing of ice and water filling resonance (Anandakrishnan and Alley, 1997).

The hybrid events tend to arrive near Station 236 first (Figure 7a). We grid search the source locations with maximal stacked normalized waveform envelopes of all the stations. Due to the geometry of the array and the low signal-to-noise ratio at the NW–SE section, only a few high-quality events can be reliably located. Figure 8a shows an example with an optimal location (76.4°, -69.48°) near the Dalk Glacier grounding line. The location histogram of the 45 high-quality hybrid events is shown as Figure 8b. It shows that the hybrid events could be from the grounding zone that connects grounded ice sheet and floating ice shelf.

These observations, together with the fortnight spring tide modulation, lead to the following hypothetical scenario. The floating ice on the seaside of the grounding line is subject to rising and falling tides, whereas the other side is roughly fixed on the bedrock. The tide-modulated stresses are concentrated at the top and bottom of the glacier near the grounding line, eventually causing ice fatigue and fracturing (Barruol et al., 2013; Begeman et al., 2020). The fractures allow sudden water inflow, either from surface meltwater or underneath sea water, leading to low-frequency and lasting

297 resonance. Hence, these hybrid events represent areas of weakness near the grounding
298 line of Dalk Glacier, similar to events observed in other glacial grounded zones of
299 East Antarctica (Barruol et al., 2013; Hammer et al., 2015; Lombardi et al., 2016;
300 Minowa et al., 2019).
301
302 Another subgroup with only low-frequency energy shows consistent propagation from
303 north to south (Figure 7b). These events were likely from the far north, and
304 attenuation could explain the absence of precursory high-frequency energy. These
305 signals could be hybrid events at the ice rumple near the front of Dalk glacier (Chen et
306 al., 2020) and/or ice calving from the glacier terminus in the north. Seismic waves of
307 calving events typically have durations > 5-30 s, energy peaks at 1-3 Hz, long
308 propagation distances and faint body-wave arrivals (Wolf and Davies, 1986; Qamar,
309 1988; O'Neel and Pfeffer, 2007). In fact, Landsat 8 recorded cracking and calving
310 activities near the ice tongue of the Amery Ice Shelf to the glacier northern terminus
311 during the same period of time (Figure 9). The breakup of ice chunks, the rotation and
312 interaction of falling icebergs with the sea surface could effectively generate the
313 observed low-frequency signals (Qamar, 1988; Bartholomaus et al., 2012).
314
315 **5.3. Potentials and limitations**
316 Our results confirm the efficiency of unsupervised deep clustering in discovering
317 different types of glacial seismic signals. With similar methods, Jenkins et al. (2021)
318 limited their analysis to 3-20 Hz and observed seismicity correlating with diurnal
319 spring tides at stations around grounding lines and iceberg calving near the ice shelves
320 front. We expand the analysis up to 250 Hz and observe high frequency icequakes and
321 their diurnal variations with temperature.
322
323 Different source processes associated with glacier dynamics call for a generalizable
324 detection and classification method. Unsupervised clustering is advantageous in that it
325 does not require preexisting labels, thus serving as a preliminary solution for data
326 inspection. However, the autoencoder requires the input spectrograms to have fixed

time lengths, which is unable to cover the wide range of glacial event durations. How to process events with different time scales remains challenging. The other issue is how to determine the preset number of clusters. We adopt 50 to overly divide the data and manually merge them into three groups. A simple preset three clusters cannot produce the same results, as the spectrogram residuals cannot fully capture perceptual similarity. For example, an event at 80 Hz is spectrally similar to another event at 90 Hz, but their spectrogram residual would be very large. These limitations need to be taken into consideration in applications of unsupervised deep clustering.

Open Research Statement

The seismic event waveform data used in this study were available via zenodo (doi: 10.5281/zenodo.7601524).

Acknowledgements

This research was supported by the National Key R&D Program of China (No. 2021YFC3000700 and 2022YFC3005602) and the National Natural Science Foundation of China (No. 42274063 and 41974044).

345 **Reference**

346 Agnew, D., 2012, SPOTL: Some programs for ocean-tide loading, 96–8.

347 Allstadt, K., and S. D. Malone, 2014, Swarms of repeating stick-slip icequakes
348 triggered by snow loading at Mount Rainier volcano, Journal of Geophysical
349 Research: Earth Surface, 119, no. 5, 1180–1203, doi: 10.1002/2014JF003086.

350 Anandakrishnan, S., and R. B. Alley, 1997, Tidal forcing of basal seismicity of ice
351 stream C, West Antarctica, observed far inland, Journal of Geophysical
352 Research: Solid Earth, 102, no. B7, 15183–15196, doi: 10.1029/97JB01073.

353 Anandakrishnan, S., and C. R. Bentley, 1993, Micro-earthquakes beneath Ice Streams
354 B and C, West Antarctica: observations and implications, Journal of
355 Glaciology, 39, no. 133, 455–462, doi: 10.3189/S0022143000016348.

356 Barruol, G., E. Cordier, J. Bascou, F. R. Fontaine, B. Legrésy, and L. Lescarmontier,
357 2013, Tide-induced microseismicity in the Mertz glacier grounding area, East
358 Antarctica, Geophysical Research Letters, 40, no. 20, 5412–5416, doi:
359 10.1002/2013GL057814.

360 Bartholomaus, T. C., C. F. Larsen, S. O'Neel, and M. E. West, 2012, Calving
361 seismicity from iceberg–sea surface interactions, Journal of Geophysical
362 Research: Earth Surface, 117, no. F4, doi: 10.1029/2012JF002513.

363 Bažant, Z. P., 1992, Large-scale thermal bending fracture of sea ice plates, J. Geophys.
364 Res., 97, no. C11, 17739–17751, doi: 10.1029/92JC00816.

365 Begeman, C. B., S. Tulaczyk, L. Padman, M. King, M. R. Siegfried, T. O. Hodson,
366 and H. A. Fricker, 2020, Tidal Pressurization of the Ocean Cavity Near an
367 Antarctic Ice Shelf Grounding Line, Journal of Geophysical Research: Oceans,
368 125, no. 4, e2019JC015562, doi: 10.1029/2019JC015562.

369 Bintanja, R., 1999, On the glaciological, meteorological, and climatological
370 significance of Antarctic blue ice areas, Reviews of Geophysics, 37, no. 3,
371 337–359, doi: 10.1029/1999RG900007.

372 Bøggild, C. E., J.-G. Winther, K. Sand, and H. Elvehøy, 1995, Sub-surface melting in
373 blue-ice fields in Dronning Maud Land, Antarctica: observations and
374 modelling, Ann. Glaciol., 21, 162–168, doi: 10.3189/S0260305500015767.

375 Boronina, A., S. Popov, G. Pryakhina, A. Chetverova, E. Ryzhova, and S. Grigoreva,
376 2021, Formation of a large ice depression on Dålk Glacier (Larsemann Hills,
377 East Antarctica) caused by the rapid drainage of an englacial cavity, J. Glaciol.,
378 67, no. 266, 1121–1136, doi: 10.1017/jog.2021.58.
379 Butkovich, T. R., 1959, Thermal Expansion of Ice, Journal of Applied Physics, 30, no.
380 3, 350–353, doi: 10.1063/1.1735166.
381 Chen, Y., 2018, Fast waveform detection for microseismic imaging using
382 unsupervised machine learning, Geophysical Journal International, 215, no. 2,
383 1185–1199, doi: 10.1093/gji/ggy348.
384 Chen, Y., C. Zhou, S. Ai, Q. Liang, L. Zheng, R. Liu, and H. Lei, 2020, Dynamics of
385 Dalk Glacier in East Antarctica Derived from Multisource Satellite
386 Observations Since 2000, Remote Sensing, 12, no. 11, 1809, doi:
387 10.3390/rs12111809.
388 Chouet, B. A., 1996, Long-period volcano seismicity: its source and use in eruption
389 forecasting, Nature, 380, no. 6572, 309–316, doi: 10.1038/380309a0.
390 Cook, C. P. et al., 2013, Dynamic behaviour of the East Antarctic ice sheet during
391 Pliocene warmth, 9, Nature Geosci, 6, no. 9, 765–769, doi: 10.1038/ngeo1889.
392 Cui, X., Z. Li, and H. Huang, 2021, Subdivision of Seismicity Beneath the Summit
393 Region of Kilauea Volcano: Implications for the Preparation Process of the
394 2018 Eruption, Geophysical Research Letters, 48, no. 20, e2021GL094698,
395 doi: 10.1029/2021GL094698.
396 Danesi, S., S. Bannister, and A. Morelli, 2007, Repeating earthquakes from rupture of
397 an asperity under an Antarctic outlet glacier, Earth and Planetary Science
398 Letters, 253, no. 1, 151–158, doi: 10.1016/j.epsl.2006.10.023.
399 Davis, C. H., Y. Li, J. R. McConnell, M. M. Frey, and E. Hanna, 2005, Snowfall-
400 Driven Growth in East Antarctic Ice Sheet Mitigates Recent Sea-Level Rise,
401 Science, 308, no. 5730, 1898–1901, doi: 10.1126/science.1110662.
402 DeConto, R. M., and D. Pollard, 2016, Contribution of Antarctica to past and future
403 sea-level rise, 7596, Nature, 531, no. 7596, 591–597, doi:
404 10.1038/nature17145.

405 Deichmann, N., J. Ansorge, F. Scherbaum, A. Aschwanden, F. Bernard, and G. H.
406 Gudmundsson, 2000, Evidence for deep icequakes in an Alpine glacier, Ann.
407 Glaciol., 31, 85–90, doi: 10.3189/172756400781820462.
408 Dutton, A., A. E. Carlson, A. J. Long, G. A. Milne, P. U. Clark, R. DeConto, B. P.
409 Horton, S. Rahmstorf, and M. E. Raymo, 2015, Sea-level rise due to polar ice-
410 sheet mass loss during past warm periods, Science, 349, no. 6244, aaa4019,
411 doi: 10.1126/science.aaa4019.
412 Ekström, G., M. Nettles, and G. A. Abers, 2003, Glacial Earthquakes, Science, 302,
413 no. 5645, 622–624, doi: 10.1126/science.1088057.
414 Frankinet, B., T. Lecocq, and T. Camelbeeck, 2021, Wind-induced seismic noise at
415 the Princess Elisabeth Antarctica Station, The Cryosphere, 15, no. 10, 5007–
416 5016, doi: 10.5194/tc-15-5007-2021.
417 Greenbaum, J. S. et al., 2015, Ocean access to a cavity beneath Totten Glacier in East
418 Antarctica, 4, Nature Geosci, 8, no. 4, 294–298, doi: 10.1038/ngeo2388.
419 Guo, J. et al., 2022, Ground-penetrating radar survey of subsurface features at the
420 margin of ice sheet, East Antarctica, Journal of Applied Geophysics, 206,
421 104816, doi: 10.1016/j.jappgeo.2022.104816.
422 Guo, X., L. Gao, X. Liu, and J. Yin, 2017, Improved Deep Embedded Clustering with
423 Local Structure Preservation, in *Proceedings of the Twenty-Sixth International*
424 *Joint Conference on Artificial Intelligence* Melbourne, Australia, International
425 Joint Conferences on Artificial Intelligence Organization, 1753–1759.
426 Hammer, C., M. Ohrnberger, and V. Schlindwein, 2015, Pattern of cryospheric
427 seismic events observed at Ekström Ice Shelf, Antarctica, Geophysical
428 Research Letters, 42, no. 10, 3936–3943, doi: 10.1002/2015GL064029.
429 Hugonnet, R. et al., 2021, Accelerated global glacier mass loss in the early twenty-
430 first century, 7856, Nature, 592, no. 7856, 726–731, doi: 10.1038/s41586-021-
431 03436-z.
432 Jenkins, W. F., P. Gerstoft, M. Bianco, and P. D. Bromirski, 2021, Unsupervised
433 Deep Clustering of Seismic Data: Monitoring the Ross Ice Shelf, Antarctica,
434 preprint, Geophysics.

435 Johnson, C. W., H. Meng, F. Vernon, and Y. Ben-Zion, 2019, Characteristics of
436 Ground Motion Generated by Wind Interaction With Trees, Structures, and
437 Other Surface Obstacles, Journal of Geophysical Research: Solid Earth, 124,
438 no. 8, 8519–8539, doi: 10.1029/2018JB017151.
439 Köhler, A., M. Ohrnberger, and F. Scherbaum, 2010, Unsupervised pattern
440 recognition in continuous seismic wavefield records using Self-Organizing
441 Maps: Unsupervised seismic pattern recognition, Geophysical Journal
442 International, 182, no. 3, 1619–1630, doi: 10.1111/j.1365-246X.2010.04709.x.
443 Kramer, M. A., 1991, Nonlinear principal component analysis using autoassociative
444 neural networks, AIChE Journal, 37, no. 2, 233–243, doi:
445 10.1002/aic.690370209.
446 Lipovsky, B. P., and E. M. Dunham, 2016, Tremor during ice-stream stick slip, The
447 Cryosphere, 10, no. 1, 385–399, doi: 10.5194/tc-10-385-2016.
448 Lombardi, D., L. Benoit, T. Camelbeeck, O. Martin, C. Meynard, and C. Thom, 2016,
449 Bimodal pattern of seismicity detected at the ocean margin of an Antarctic ice
450 shelf, Geophys. J. Int., 206, no. 2, 1375–1381, doi: 10.1093/gji/ggw214.
451 Lombardi, D., I. Gorodetskaya, G. Barruol, and T. Camelbeeck, 2019, Thermally
452 induced icequakes detected on blue ice areas of the East Antarctic ice sheet,
453 Annals of Glaciology, 60, no. 79, 45–56, doi: 10.1017/aog.2019.26.
454 MacAyeal, D. R., A. F. Banwell, E. A. Okal, J. Lin, I. C. Willis, B. Goodsell, and G. J.
455 MacDonald, 2019, Diurnal seismicity cycle linked to subsurface melting on an
456 ice shelf, Annals of Glaciology, 60, no. 79, 137–157, doi:
457 10.1017/aog.2018.29.
458 Minowa, M., E. A. Podolskiy, and S. Sugiyama, 2019, Tide-modulated ice motion
459 and seismicity of a floating glacier tongue in East Antarctica, Annals of
460 Glaciology, 60, no. 79, 57–67, doi: 10.1017/aog.2019.25.
461 Mohajerani, Y., I. Velicogna, and E. Rignot, 2018, Mass Loss of Totten and Moscow
462 University Glaciers, East Antarctica, Using Regionally Optimized GRACE
463 Mascons, Geophysical Research Letters, 45, no. 14, 7010–7018, doi:
464 10.1029/2018GL078173.

Mousavi, S. M., W. Zhu, W. Ellsworth, and G. Beroza, 2019, Unsupervised Clustering of Seismic Signals Using Deep Convolutional Autoencoders, IEEE Geosci. Remote Sensing Lett., 16, no. 11, 1693–1697, doi: 10.1109/LGRS.2019.2909218.

Mucciarelli, M., M. R. Gallipoli, D. Di Giacomo, F. Di Nota, and E. Nino, 2005, The influence of wind on measurements of seismic noise, Geophysical Journal International, 161, no. 2, 303–308, doi: 10.1111/j.1365-246X.2004.02561.x.

Neave, K. G., and J. C. Savage, 1970a, Icequakes on the Athabasca Glacier, Journal of Geophysical Research (1896-1977), 75, no. 8, 1351–1362, doi: 10.1029/JB075i008p01351.

Neave, K. G., and J. C. Savage, 1970b, Icequakes on the Athabasca Glacier, Journal of Geophysical Research (1896-1977), 75, no. 8, 1351–1362, doi: 10.1029/JB075i008p01351.

O'Neel, S., and W. T. Pfeffer, 2007, Source mechanics for monochromatic icequakes produced during iceberg calving at Columbia Glacier, AK, Geophysical Research Letters, 34, no. 22, doi: 10.1029/2007GL031370.

Osten-Woldenburg, H. V. D., 1990, Icequakes On Ekström Ice Shelf Near Atka Bay, Antarctica*, Journal of Glaciology, 36, no. 122, 31–36, doi: 10.3189/S0022143000005517.

Padman, L., H. A. Fricker, R. Coleman, S. Howard, and L. Erofeeva, 2002, A new tide model for the Antarctic ice shelves and seas, Annals of Glaciology, 34, 247–254, doi: 10.3189/172756402781817752.

Paolo, F. S., H. A. Fricker, and L. Padman, 2015, Volume loss from Antarctic ice shelves is accelerating, Science, 348, no. 6232, 327–331, doi: 10.1126/science.aaa0940.

Podolskiy, E. A., and F. Walter, 2016, Cryoseismology: CRYOSEISMOLOGY, Rev. Geophys., 54, no. 4, 708–758, doi: 10.1002/2016RG000526.

Qamar, A., 1988, Calving icebergs: A source of low-frequency seismic signals from Columbia Glacier, Alaska, Journal of Geophysical Research: Solid Earth, 93, no. B6, 6615–6623, doi: 10.1029/JB093iB06p06615.

Reynolds, D.A., 2009, Gaussian mixture models. Encyclopedia of biometrics, 741(659-663).

Rignot, E., J. L. Bamber, M. R. van den Broeke, C. Davis, Y. Li, W. J. van de Berg, and E. van Meijgaard, 2008, Recent Antarctic ice mass loss from radar interferometry and regional climate modelling, 2, Nature Geosci, 1, no. 2, 106–110, doi: 10.1038/ngeo102.

Rignot, E., J. Mouginot, B. Scheuchl, M. van den Broeke, M. J. van Wessem, and M. Morlighem, 2019, Four decades of Antarctic Ice Sheet mass balance from 1979–2017, Proceedings of the National Academy of Sciences, 116, no. 4, 1095–1103, doi: 10.1073/pnas.1812883116.

Roeoesli, C., A. Helmstetter, F. Walter, and E. Kissling, 2016, Meltwater influences on deep stick-slip icequakes near the base of the Greenland Ice Sheet, Journal of Geophysical Research: Earth Surface, 121, no. 2, 223–240, doi: 10.1002/2015JF003601.

Röösli, C., F. Walter, S. Husen, L. C. Andrews, M. P. Lüthi, G. A. Catania, and E. Kissling, 2014, Sustained seismic tremors and icequakes detected in the ablation zone of the Greenland ice sheet, Journal of Glaciology, 60, no. 221, 563–575, doi: 10.3189/2014JoG13J210.

Seydoux, L., R. Balestriero, P. Poli, M. de Hoop, M. Campillo, and R. Baraniuk, 2020, Clustering earthquake signals and background noises in continuous seismic data with unsupervised deep learning, 1, Nat Commun, 11, no. 1, 3972, doi: 10.1038/s41467-020-17841-x.

Shen, Q., H. Wang, C. K. Shum, L. Jiang, H. T. Hsu, and J. Dong, 2018, Recent high-resolution Antarctic ice velocity maps reveal increased mass loss in Wilkes Land, East Antarctica, 1, Sci Rep, 8, no. 1, 4477, doi: 10.1038/s41598-018-22765-0.

Shepherd, A. et al., 2018, Mass balance of the Antarctic Ice Sheet from 1992 to 2017, 7709, Nature, 558, no. 7709, 219–222, doi: 10.1038/s41586-018-0179-y.

Shepherd, A., and D. Wingham, 2007, Recent Sea-Level Contributions of the Antarctic and Greenland Ice Sheets, Science, 315, no. 5818, 1529–1532, doi:

525 10.1126/science.1136776.
526 Stokes, C. R. et al., 2022, Response of the East Antarctic Ice Sheet to past and future
527 climate change, 7922, Nature, 608, no. 7922, 275–286, doi: 10.1038/s41586-
528 022-04946-0.
529 Walter, F., N. Deichmann, and M. Funk, 2008, Basal icequakes during changing
530 subglacial water pressures beneath Gornergletscher, Switzerland, Journal of
531 Glaciology, 54, no. 186, 511–521, doi: 10.3189/002214308785837110.
532 Wang, L., J. L. Davis, and I. M. Howat, 2021, Complex Patterns of Antarctic Ice
533 Sheet Mass Change Resolved by Time-Dependent Rate Modeling of GRACE
534 and GRACE Follow-On Observations, Geophysical Research Letters, 48, no.
535 1, e2020GL090961, doi: 10.1029/2020GL090961.
536 Wilson, D. J., R. A. Bertram, E. F. Needham, T. van de Flierdt, K. J. Welsh, R. M.
537 McKay, A. Mazumder, C. R. Riesselman, F. J. Jimenez-Espejo, and C. Escutia,
538 2018, Ice loss from the East Antarctic Ice Sheet during late Pleistocene
539 interglacials, 7723, Nature, 561, no. 7723, 383–386, doi: 10.1038/s41586-018-
540 0501-8.
541 Winberry, J. P., S. Anandakrishnan, R. B. Alley, R. A. Bindschadler, and M. A. King,
542 2009, Basal mechanics of ice streams: Insights from the stick-slip motion of
543 Whillans Ice Stream, West Antarctica, Journal of Geophysical Research: Earth
544 Surface, 114, no. F1, doi: 10.1029/2008JF001035.
545 Winter, K., D. Lombardi, A. Diaz-Moreno, and R. Bainbridge, 2021, Monitoring
546 Icequakes in East Antarctica with the Raspberry Shake, Seismological
547 Research Letters, 92, no. 5, 2736–2747, doi: 10.1785/0220200483.
548 Withers, M. M., R. C. Aster, C. J. Young, and E. P. Chael, 1996, High-frequency
549 analysis of seismic background noise as a function of wind speed and shallow
550 depth, Bulletin of the Seismological Society of America, 86, no. 5, 1507–1515,
551 doi: 10.1785/BSSA0860051507.
552 Wolf, L. W., and J. N. Davies, 1986, Glacier-generated earthquakes from Prince
553 William Sound, Alaska, Bulletin of the Seismological Society of America, 76,
554 no. 2, 367–379, doi: 10.1785/BSSA0760020367.

555 Zoet, L. K., B. Carpenter, M. Scuderi, R. B. Alley, S. Anandakrishnan, C. Marone,
556 and M. Jackson, 2013, The effects of entrained debris on the basal sliding
557 stability of a glacier, Journal of Geophysical Research: Earth Surface, 118, no.
558 2, 656–666, doi: 10.1002/jgrf.20052.
559 Zwally, H. J., M. B. Giovinetto, J. Li, H. G. Cornejo, M. A. Beckley, A. C. Brenner, J.
560 L. Saba, and D. Yi, 2005, Mass changes of the Greenland and Antarctic ice
561 sheets and shelves and contributions to sea-level rise: 1992–2002, Journal of
562 Glaciology, 51, no. 175, 509–527, doi: 10.3189/172756505781829007.
563
564

Figures

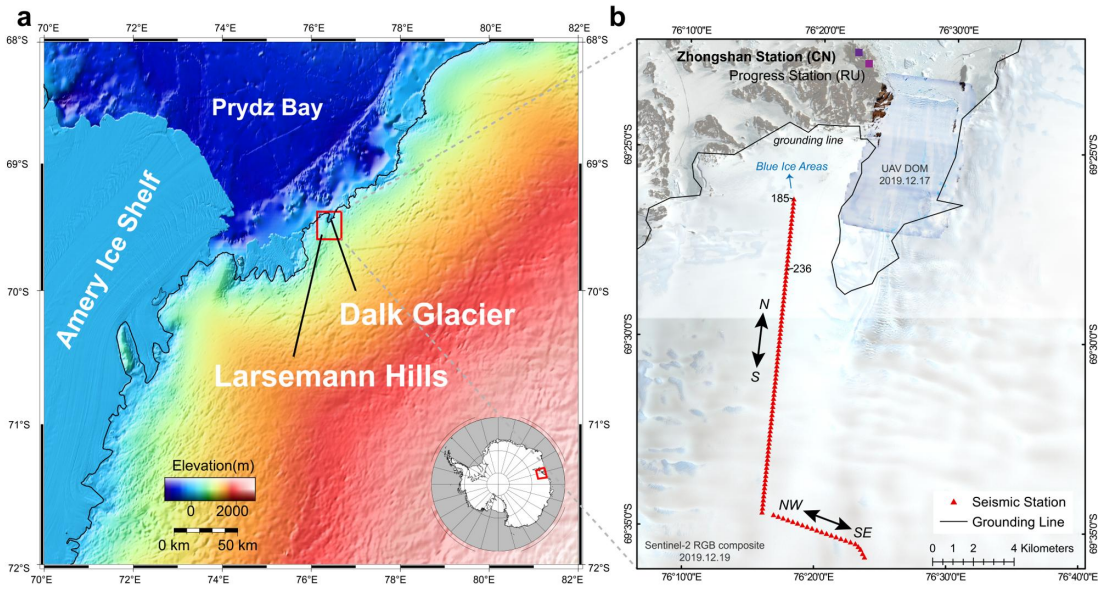

Figure 1. (a) The Larsemann Hills and Dalk Glacier on the east side of the Amery Ice Shelf, East Antarctica. The black line marks the grounding line, where the grounding glacier transitions to the floating ice shelf. (b) Study area and seismic array. Background is a satellite image acquired by Sentinel-2 with embedded Dalk Glacier by Unmanned Aerial Vehicle (UAV). Red triangles represent 100 three-component short-period seismometers from 6 Dec 2019 to 2 Jan 2020. Purple squares mark China's Zhongshan Station and Russia's Progress Station. Around Station 185 there are some blue ice areas where the surface snow layer is absent and the albedo is relatively lower.

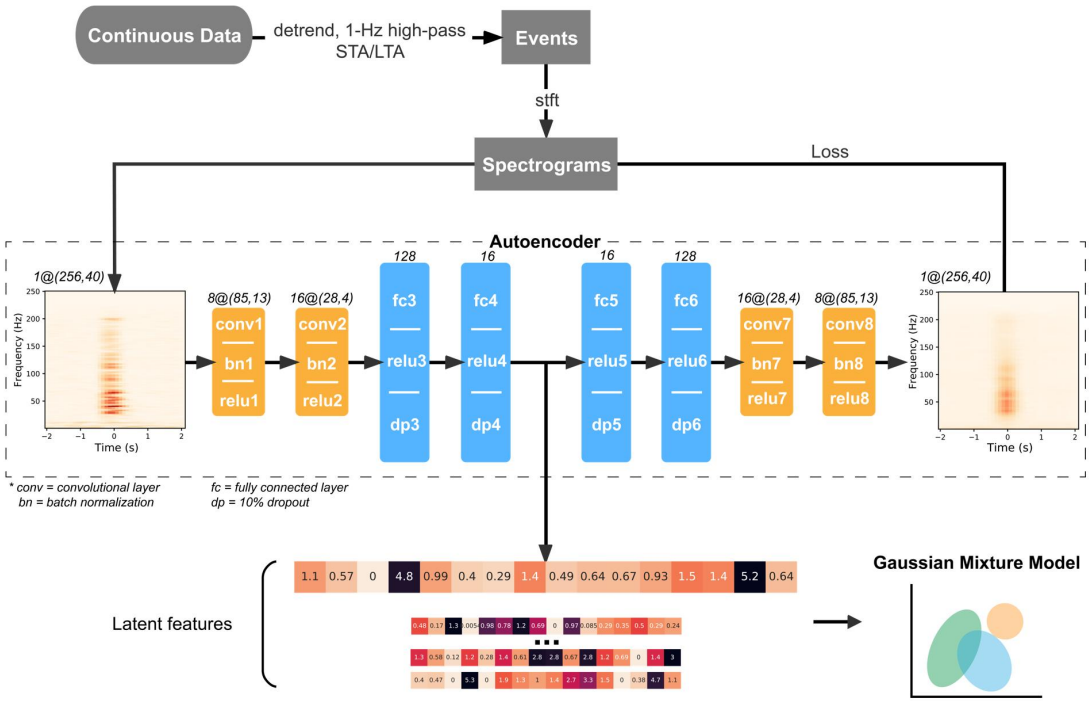

Figure 2. Workflow of seismic event detection and clustering: short-term-average/long-term-average detection, an autoencoder for feature extraction, a Gaussian mixture model for clustering. The autoencoder is trained with mean square error loss between the input and output spectrograms. The latent feature dimension is 16. The Gaussian mixture model has a preset parameter of 50 clusters which are then merged manually.

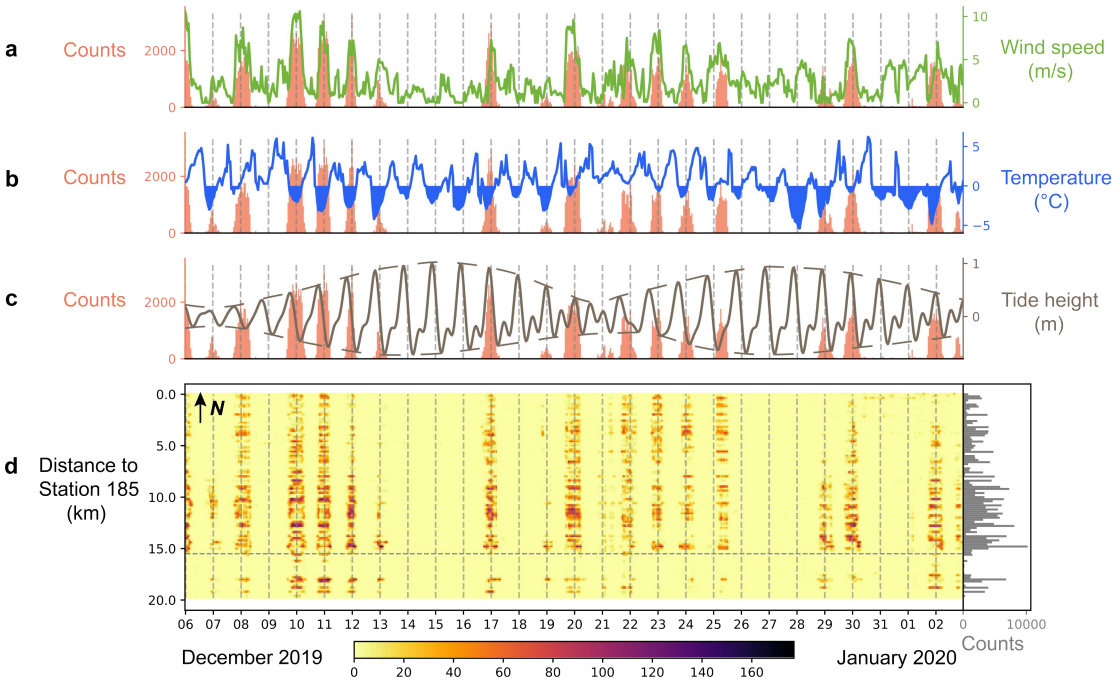

586

587 **Figure 3.** Hourly counts of Cluster A events compared with environmental
588 measurements of wind speed (a), temperature (b) recorded at Zhongshan Station, and
589 simulated local tide level (c). (d) Spatiotemporal distribution of Cluster A events. On
590 the right is the sum on each station. The grey horizontal dashed line marks the array
591 transition for N-S to NW-SE. X axis is UTC time (local time is 5 hours behind).

592

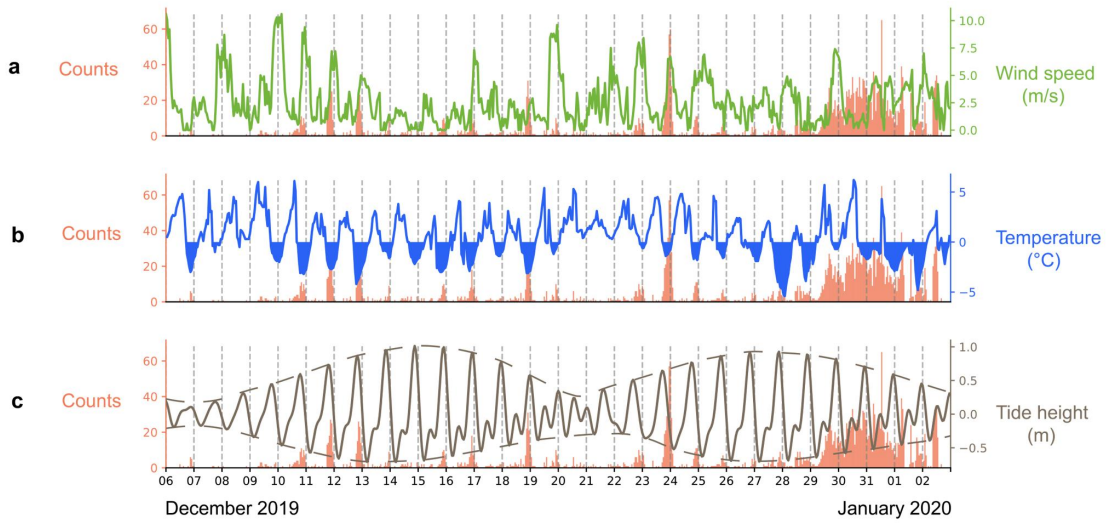

Figure 4. Hourly counts of Cluster B events on Station 185 compared with environmental measurements of wind speed (a), temperature (b) recorded at Zhongshan Station, and simulated local tide level (c). X axis is UTC time (local time is 5 hours behind).

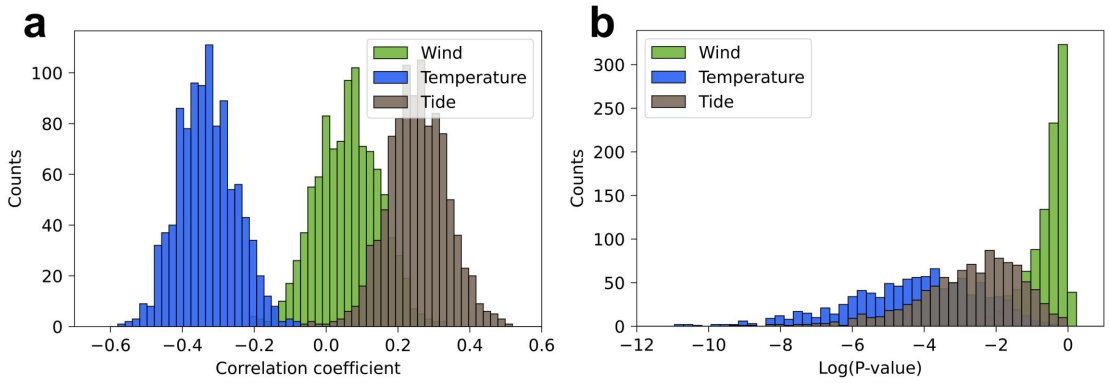

599

600 **Figure 5.** Histograms of Spearman correlation coefficients (a) and *p* values (b)
601 between Cluster B events on Station 185 and environmental forces from 1,000 times
602 of bootstrapping.

603

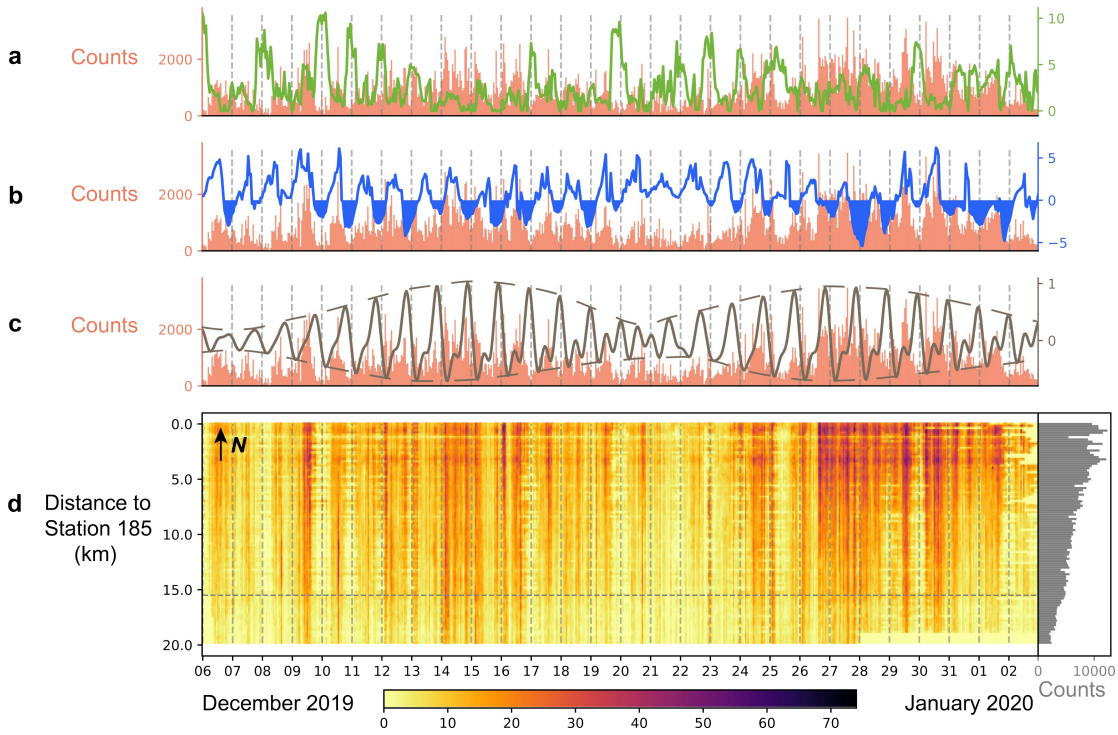

604

605 **Figure 6.** Hourly counts of Cluster C events compared with environmental
606 measurements of wind speed (a), temperature (b) recorded at Zhongshan Station, and
607 simulated local tide level (c). (d) Spatiotemporal distribution of Cluster C events. On
608 the right is the sum on each station. The grey horizontal dashed line marks the array
609 transition for N-S to NW-SE. X axis is UTC time (local time is 5 hours behind). Gaps
610 for some stations in final days represent no effective data available.

611

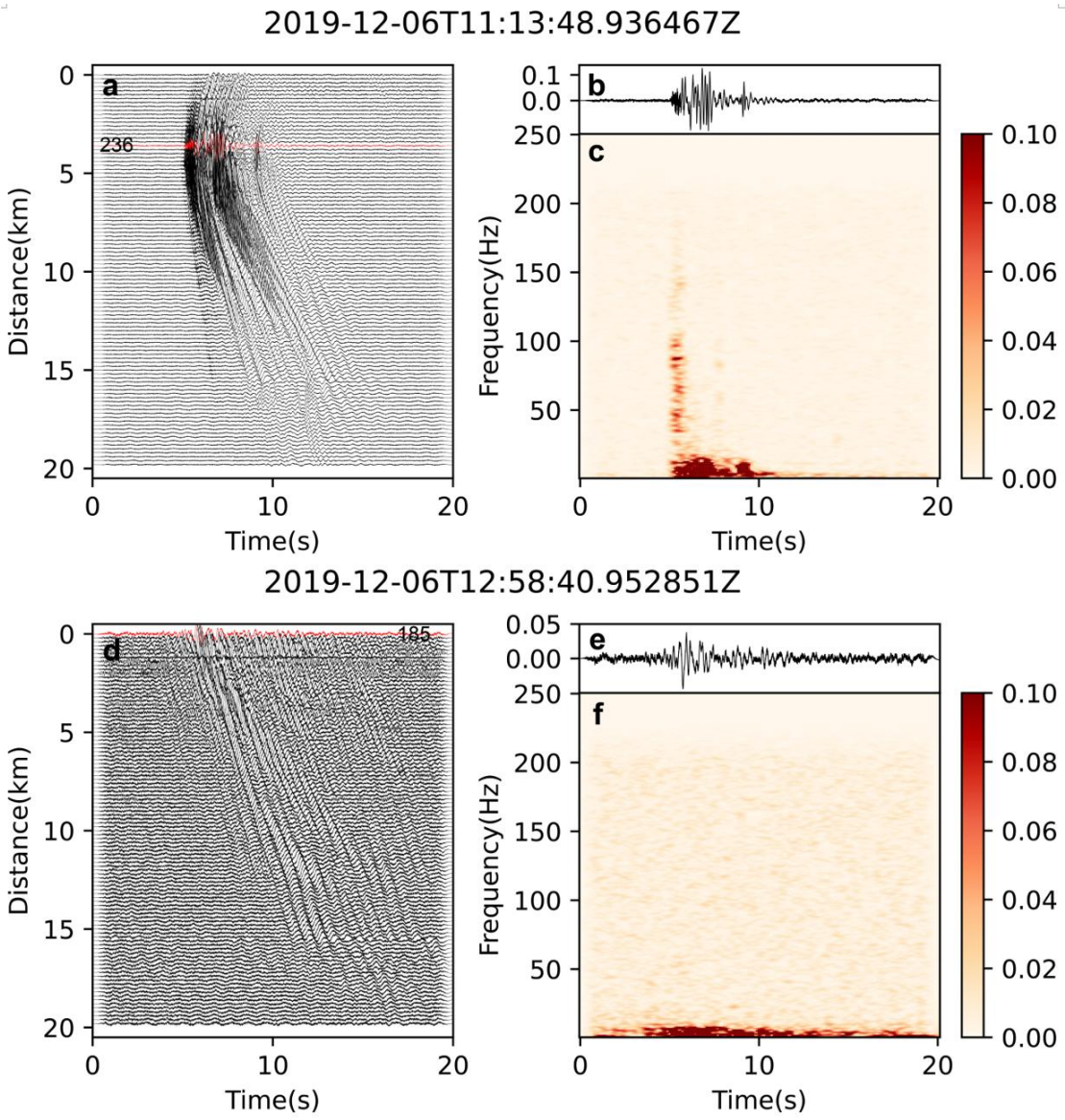

Figure 7. Two representative examples of Cluster C events. (a) is an example with high-frequency first arrival in the middle of the array. (b) and (c) show the waveform and its normalized spectrogram on the station with the earliest arrival. (d) is another example with dominant low-frequency waves traveling from the north. (e) and (f) show the waveform and its normalized spectrogram on the northmost station.

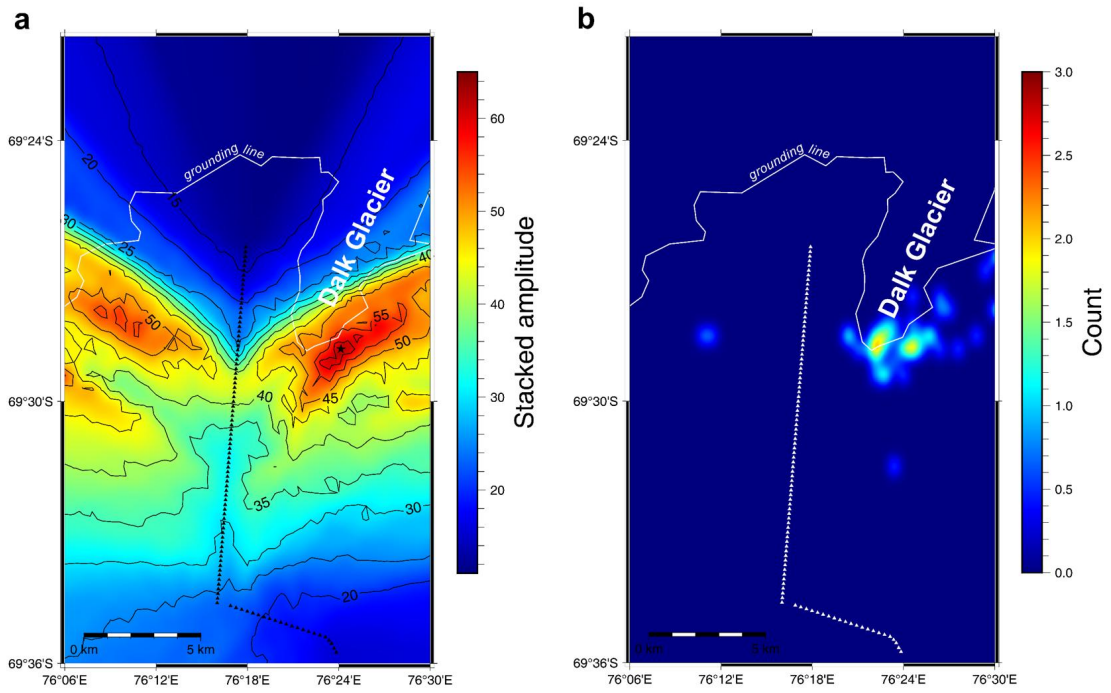

Figure 8. Grid search results for the hybrid events location. (a) Stacked amplitudes of the case in Figure 7a. The black star marks the most plausible focus location. Black triangles are seismic stations. White lines mark the grounding line of Dalk Glacier. (b) Focus location distribution for 45 high-quality events. The peak occurs along the grounding line.

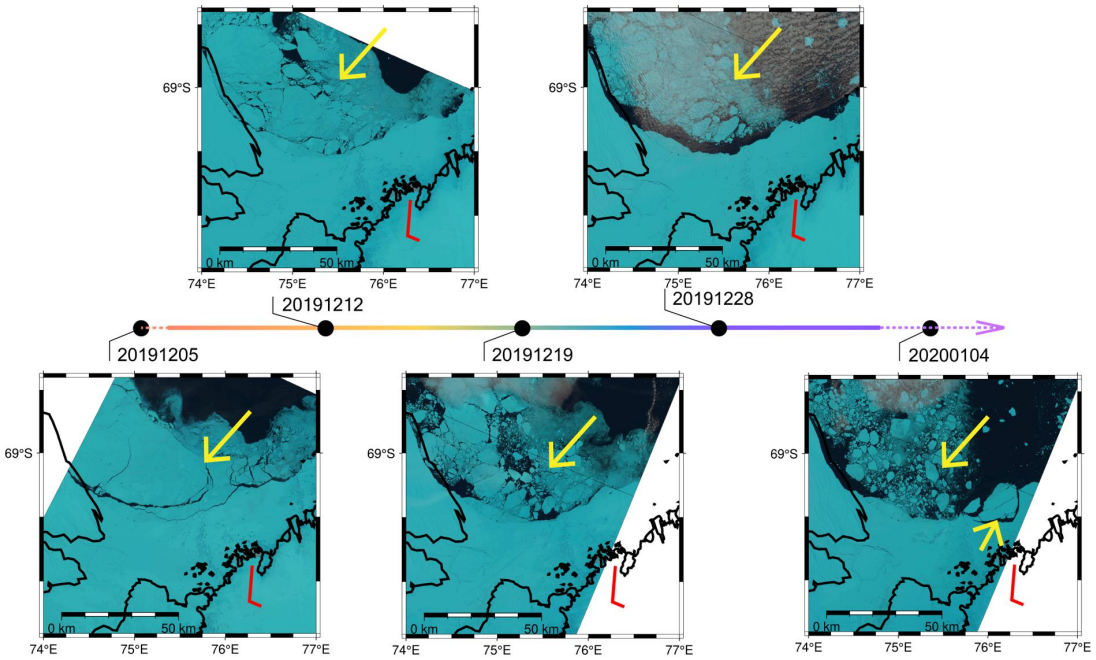

Figure 9. Weekly satellite imagery around the study area in the same period. Yellow arrows highlight the rapidly changing ice (i.e. breakup and drifting). The red line is the seismic array. The solid part of the time line represents the operation period of our seismic array.

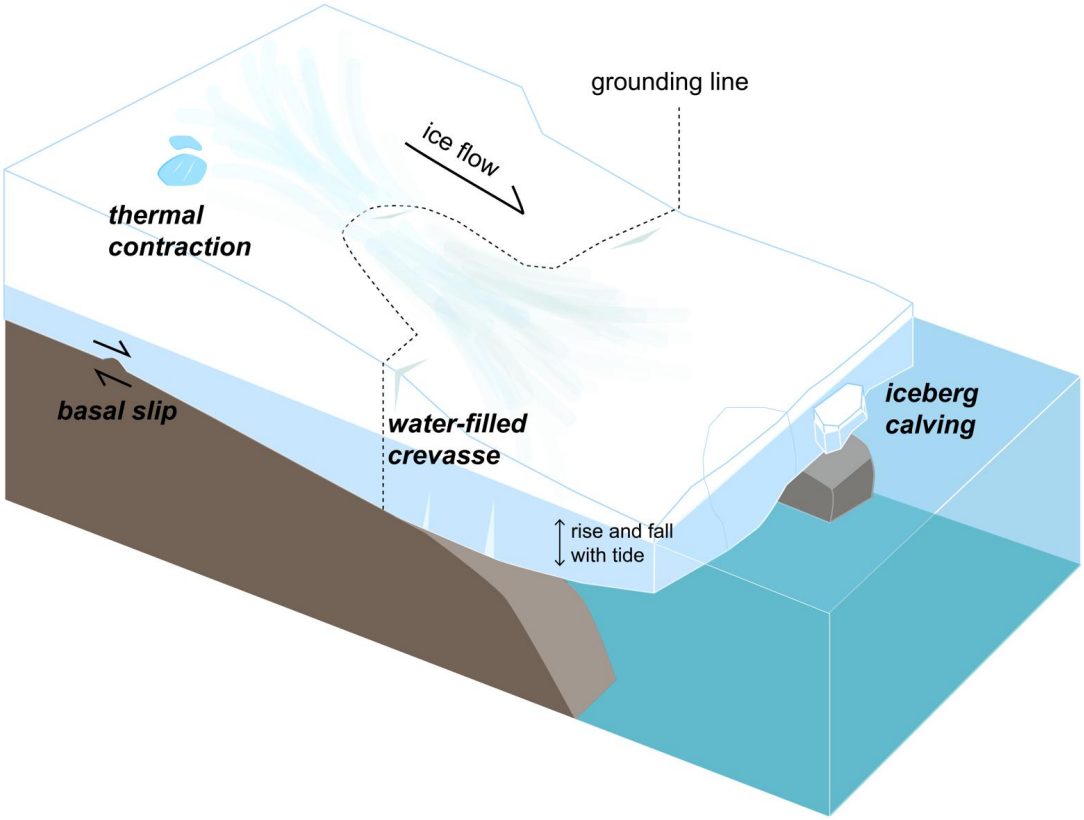

631

632 **Figure 10.** Carton illustration of possible mechanisms for the diverse seismic signals

633 near Dalk Glacier in East Antartica.

634